PAPER • **OPEN ACCESS**

Investigating the effect of varying multi-pass welding sequence and plate thickness with manhole on plate distortion

Journal of Physics: Conference Series **3058** (2025) 012020 doi:10.1088/1742-6596/3058/1/012020

Investigating the effect of varying multi-pass welding sequence and plate thickness with manhole on plate distortion

Ahmed B Salman[1], Abd Elhamid I Gomaa[1] and Sallam A Kourietm[1]

[1] Mechanical Department, Faculty of Engineering, Alexandria University, Egypt
E-mail: ahmed.bassem@alexu.edu.eg

Abstract. Welding methods are crucial for component assembly in various industries, yet many forms of deformation due to the irregular thermal expansion and contraction are noticed, affecting their dimensions and alignment. This paper presents a set of experimental models alongside a simulation for the welding process utilizing a thermo elastic plastic approach with COMSOL Multiphysics 6.0, yielding results that closely align with each other. The study adopts multi-pass fillet welding instead of the traditional single-pass method. This is done by flux-cored arc welding under specific constraints. The study examines the mutual effects of varying welding sequences and plate thicknesses, without altering stiffener geometrical configuration. The focus is on distortion reduction in a flat bar stiffened plate with a manhole opening. This plate is considered as one of the tank faces used in the ship industry. The research successfully determines vertical displacement due to distortion. Findings also indicate that optimizing welding sequences is essential for different thicknesses, particularly thicker ones, which are significantly affected by sequence variation more than thinner plates.

1. Introduction

In numerous industries, welding techniques are essential to the successful assembly of components, yet improper welding sequences can exacerbate distortions [1-5]. Methods like the Joint Rigidity Method highlighting the importance of weld placement near the neutral axis [6]. In smaller assemblies, the direction and placement of welded stiffeners demonstrated a more significant effect on distortion than the sequencing of welding [7]. Some studies demonstrate numerically using ABAQUS [8, 9] and MSC Marc non-linear FEA solutions [10] that alterations in welding sequences aimed at minimizing distortions in ships and offshore structures. Studies demonstrate numerically and also by experimental means that single-side welding leads to greater distortion than double-side welding [11]. Deng and Murakawa [12] uncovered that ignoring optimal welding sequences could result in buckling distortion in thin, plate-structured, ship stiffened panels. Both experimental and numerical analyses indicated that reversing the welding direction [11, 13, 14] on both sides of fillet joints mitigates welding distortion. This claim is contested by Chen et al. [15], who found that simultaneous welding in one direction results in the least distortion compared to successive or bi-directional welding in stiffened panels. Chen, Shenoi [16], and Shadkam et al. [17] developed thermal elastic-plastic FEM models. These assess the impact of welding sequence and stiffener configurations on distortion. Rodrigues et al. [18] determined that a welding sequence starting from the inner stiffeners outwards with a reverse straightforward pass deposition, conducted by robotic FCAW, improved heat distribution and minimized distortion in producing 10 mm thick, longitudinally strengthened panels. Azad and Iranmanesh [19] identified that welding sequence also significantly influences temperature distribution, more than peak temperatures alone, implying that it affects the magnitude of deformation

more profoundly than residual stresses. Hammad et al. [20] asserted that a non-continuous symmetrical welding sequence, which extends from the interior outward, can minimize out-of-plane distortion. This occurs while producing the least weight of steel from alterations in flange thicknesses and widths. Tomk'ow et al. [21] found that a continuous welding sequence, in conjunction with tack welds, diminished angular distortion values.

Numerous researchers have investigated both numerically and experimentally the consequences of external restraints like clamps [22, 23] and jigs [24, 25], effectively reducing welding deformation compared to unconstrained conditions. However, they may increase residual stresses, as highlighted by Fu et al. [26]. Experimental and computational approaches indicate that the arrangement and distribution of jigs [27, 28], along with clamps and strong-backs [22, 29], aid in minimizing welding deformation. Zhang and Wang [24, 30] investigated using thermo elastic-plastic methods to show that symmetrically placed mechanical boundary conditions directly influence the reduction of distortions.

Saad-Eldeen et al. [31] conducted distortion analysis using continuous and intermittent chain welding with the shielded metal arc welding process. They found that distortion amplitude decreases as plate thickness increases and that intermittent weld has less impact on final amplitude.

This article is primarily focused on studying the reduction in z-axis deformation percentage when two different welding sequences, a straightforward pass and two sub-passes of outward motions from the centre, are performed on two distinct thick normal strength grade A marine steel plates designed with a manhole opening and reinforced with two stiffeners. Flux-cored arc welding and symmetrically distributed constraints are similarly applied for all cases. A multi-pass welding approach is utilized rather than the commonly used single-pass technique. The results of this investigation are numerically validated against experimental measurements.

2. Experimental model

This study analyzes the effects of two welding sequences on vertical displacement on one of the tank faces when the flange thickness is altered from 9 to 18 mm.

2.1. Materials Utilized

Grade A marine steel of 235 MPa minimum yield strength as per BV marine regulations is utilized for its favorable welding properties. The filler material is Hyundai Supercored 71 flux-cored wires with a diameter of 1.2 mm. It is recognized by the American Welding Society as AWS A5.20 E71-T1-C. It is selected for its compatibility in mechanical properties and chemical analysis with the base material, as detailed in tables 1 and 2, ensuring high-quality welds.

Table 1. Mechanical properties of base metal and filler material.

		Yield stress (MPa)	Tensile strength (MPa)	Elongation (%)
Base metal	Grade A	344	462	28
	Grade A (BV)	235	400-520	≥22
Filler material	Supercored 71	545	572	28
	AWS A5.20 E71T-1C	≥ 390	490-670	≥ 22

Table 2. Chemical analysis of base metal and filler material.

		C	Si	Mn	P	S	Fe
Base metal	Grade A	0.14	0.17	0.62	0.015	0.025	Rem
	Grade A (BV)	≤ 0.21	≤ 0.5	≥ 2.5xC	≤ 0.035	≤ 0.035	Rem
Filler material	Supercored 71	0.036	0.51	1.26	0.010	0.011	Rem
	AWS A5.20 E71T-1C	≤ 0.12	≤ 0.9	≤ 1.75	≤ 0.03	≤ 0.03	Rem

2.2. Preparation of test specimens and joints

Specimens are cut using a Hypertherm plasma cutting system to ensure precise dimensions. After cutting, the plate is placed on a welding table previously calibrated using a multi-line laser device FLG 70-GREEN SP Type to ensure flatness. The structure consists of a plate of dimensions as per figure 1, while its thickness varies between 9 mm and 18 mm and two flat bars of thickness 10 mm with a taper of 30° angle and 80 mm height at both ends for each stiffener. A control grid of 10 mm by 10 mm squares is drawn to facilitate temperature and distortion measurements. Joints are prepared for double-sided fillet welds at a 90° angle, with surfaces cleaned before welding. Tack welds are used to assemble the structure, which lies on the welding table between four Ø 20 studs at the plate vertices, as shown in figure 2. Locating vertices guarantees that all cases have the same coordinates.

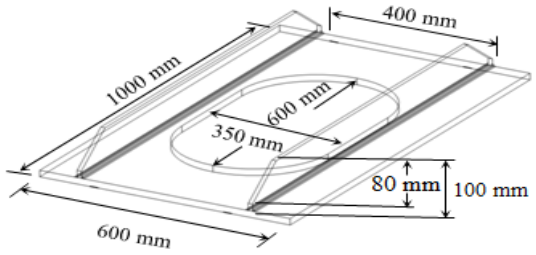

Figure 1. Model dimensions.

Figure 2. Pre-Welding Setup for the experimental model.

2.3. Welding process

Weld beads are deposited in a horizontal down-hand position. This is done using YD-500KR Panasonic MIG/MAG arc power supplies and YT-50CS Panasonic welding gun with a multi-pass flux-cored arc welding technique. Pure CO_2 serves as the shielding gas. Single bead welds are limited to a maximum leg length of 7 mm, in compliance with BV regulations. In some cases, especially with greater thicknesses, creating a 7 mm-sized leg length or more is quite challenging and could adversely affect the final structure. The two used passes parameters are detailed in table 3, with temperature monitored using a Crown infrared thermometer CT44037. It is also utilized to ensure that the inter-pass temperature is kept below 150°C before applying the additional weld pass on the same weld line. The applied heat input [32] ranges from 10.5 to 13 KJ/cm for the first pass and between 7 and 9.1 KJ/cm for the second pass and can be calculated by equation (1) as follows.

$$Q = \frac{U \times I \times \eta}{v \times 1000} \tag{1}$$

Where Q is the heat input, U is the voltage, I is the electric current, η is the welding efficiency coefficient, and v is the travel speed of the welding torch. A welding efficiency coefficient η is assumed as 0.85 for the FCAW process [15, 33].

Table 3. Welding parameters utilized in experiment.

Parameter	Value		Units
	1st pass	2nd pass	
Current	230		A
Voltage	34		V
Welding speed	5	6.5	mm/s
Gas flow rate	18		L/min
Stick-out	17		mm
CTWD	20		mm
Torch Angle	45		°

2.4. Mechanical restraints

The panel is fixed at its vertices with locator studs, fastened with nuts and grade A steel rectangular washers. Eight dogs and wedges are evenly distributed to enhance stability and minimize distortion, as shown in figure 2. After cooling to ambient temperature, restraints are removed to measure vertical displacement. It is worth noting that the effect of tack welds during assembly was not considered.

2.5. Welding sequence

The study categorizes four welding cases, as shown in table 4, based on two welding sequences conducted for both 9 and 18 mm thick flanges. This assesses the percentage reduction in vertical displacement versus thickness increase for each case. Sequence 1, S1, involves 8 weld passes, with two passes on each weld line deposited in a straightforward approach. Sequence 2, S2, the centre-out technique, involves a total of 16 sub-passes. Each of 8 passes is divided into two sub-passes. The weld bead direction is oriented at 180° for each run. The elapsed time in the welding process for each case is tabulated in table 5. The arc on time represents the actual welding duration, while inter-pass cooling time is the waiting period for the weld line to cool below inter-pass temperature. Inter-pass cleaning time comprises the time required to brush the flux out of the first run surface before depositing the second run. It also includes the grinding period computed while grinding the sub-passes starting junctions for S2 cases to ensure a sound weld. Repositioning time refers to how long the welder takes to relocate according to welding routes outlined in table 6 and illustrated in figure 2.

Table 4. Welding cases and their nomenclatures.

Case No.	Thickness	Sequence	Nomenclatures
Case 1	9 mm	S1	T9-S1
Case 2		S2	T9-S2
Case 3	18 mm	S1	T18-S1
Case 4		S2	T18-S2

Table 5. Welding sequences elapsed time.

Case	Time (min : sec)				
	Arc On	Inter-pass cooling	Inter-pass Cleaning	Repositioning	Total
T9-S1	22:03	4:48	3:02	1:36	31:29
T9-S2	24:24	-	4:49	6:17	35:30
T18-S1	22:15	4:01	2:50	1:20	30:26
T18-S2	24:06	-	4:31	6:22	34:59

Table 6. Welding sequences routes.

Sequence	Welding route
S1	A→B , B→A , C→D , D→C , E→F , F→E , G→H , H→G.
S2	W→B , X→D , Y→F, Z→H, W→A , X→C , Y→E, Z→G , W→A , X→C , Y→E, Z→G, W→B , X→D , Y→F, Z→H.

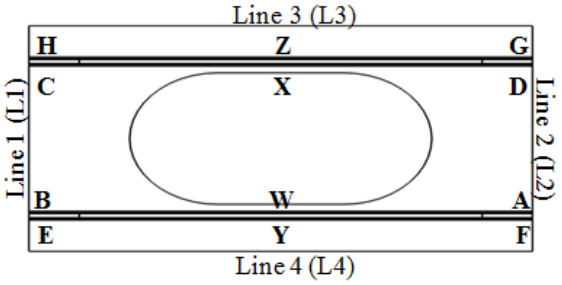

Figure 3. Lines for measurements and welding sequence steps.

2.6. Measurement procedures

2.6.1. Temperature evaluation. Temperature measurements were conducted using the CT44037 infrared thermometer. Surface temperature is measured for two nodes, T1 and T2, as shown by red dots in figure 4. This process is approximately repeated every 20 seconds, starting with the beginning of the welding process.

2.6.2. Distortion evaluation. FLG 70-GREEN SP Type device establishes a reference line for measuring vertical displacement. Measurements are taken for displacement nodes, as shown in figure 4, before and after welding, considering pre-existing geometrical inconsistencies. Knowing that, black nodes represent critical locations at edges and vertices, green nodes indicate internal measurement positions, and blue nodes points to manhole measurement spots After cooling to room temperature (25°C) under uniform air cooling [34], restraints are released, allowing the panel to develop its final deformation shape. The plate is repositioned before carrying out the second measurement as shown in figure 5. Vertical displacement is calculated by subtracting the final reading from the initial one. A vernier caliper is also used as a double-check measurement device, as seen in figure 6. The welding process is similarly applied numerically using COMSOL 6.0. This is done to compare results and establish the correlation between temperature gradients and final distortion.

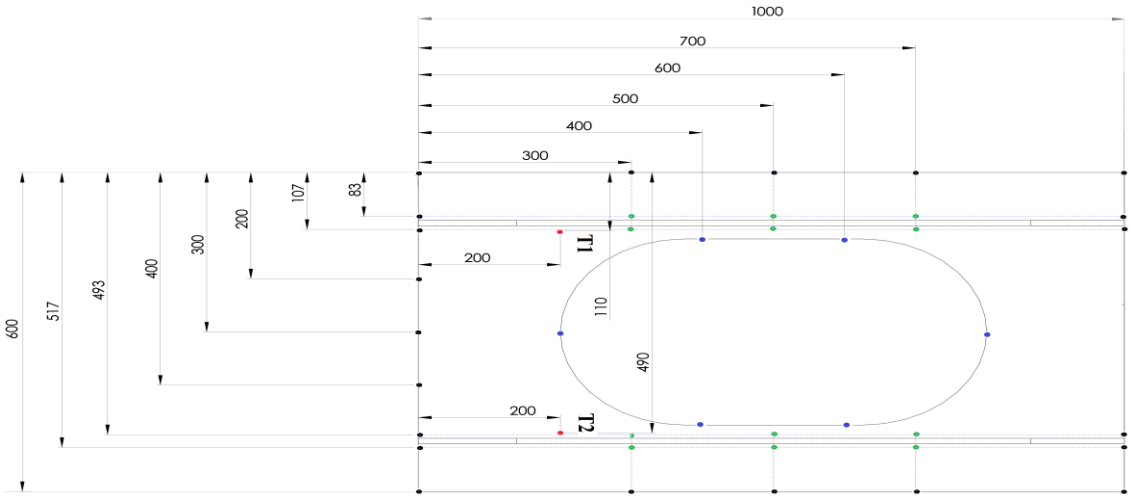

Figure 4. Measuring points location.

.

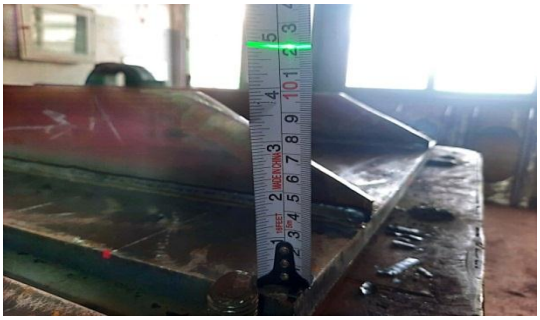

Figure 5. FLG type Laser device evaluating second measuring after constraints released.

Figure 6. Re-checking the final displacement value using a vernier caliper.

3. Simulation model for welding

The finite element method (FEM) was utilized to model temperature distribution and deformation during and after welding, effectively conserving both time and costs. Achieving an accurate simulation

is challenging, as convergence may not always be guaranteed, necessitating a focus on optimizing accuracy while disregarding unnecessary complexities.

Accounting for properties of S235JR steel as an analogue to grade A steel, as they closely resemble each other in both chemical and mechanical characteristics, was adopted for the finite element analysis [35, 36].

3.1. Analysis of thermal dynamics

To explore transient temperatures during the welding process, a non-linear partial differential equation using Fourier's law and energy conservation is solved. Equation (2) expresses the transient temperature field (T) as a function of time (t) and x, y, z spatial coordinates:

$$\rho(T)C_p(T)\frac{\partial T}{\partial t} = \frac{\partial}{\partial x}\left(k(T)\frac{\partial T}{\partial x}\right) + \frac{\partial}{\partial y}\left(k(T)\frac{\partial T}{\partial y}\right) + \frac{\partial}{\partial z}\left(k(T)\frac{\partial T}{\partial z}\right) + q \quad (2)$$

Where $\rho(T)$, $C_p(T)$ and $k(T)$ represent the temperature-dependent density, specific heat, and thermal conductivity, respectively. The volumetric heat source density q (W/m^3) denotes internal heat generation, represented by a double ellipsoidal distribution model proposed by Goldak et al. [37]. Thermal boundary conditions account for heat loss through natural convection and radiation, with coefficients set at k = 10 $W/m^2 \cdot K$ and $\alpha = 0.9$ [33], respectively.

3.2. Mechanical assessment

During the welding operation, the overall strain within the structure can be separated into several components as elastic strain, plastic strain, thermal strain, phase transformation strain, and creep strain. This study, based on thermal analysis, excludes the strain rate components attributable to phase change [38-40] and creep [41-43]. The total strain rate, $\dot{\varepsilon}^{total}$, is expressed in terms of its individual constituents for equation (3) as follows [44]:

$$\dot{\varepsilon}^{total} = \dot{\varepsilon}^{e} + \dot{\varepsilon}^{p} + \dot{\varepsilon}^{th} \quad (3)$$

Where $\dot{\varepsilon}^{e}$, $\dot{\varepsilon}^{p}$, and $\dot{\varepsilon}^{th}$ correspond to elastic strain rate, plastic strain rate, and thermal strain rate respectively.

Mechanical properties needed for structural evaluation, including temperature-dependent yield strength, young's modulus, Poisson's ratio, and thermal expansion coefficients, are adapted from literature [36] for both base and filler metals.

4. Results and discussion

Welding deformation is primarily classified into shrinkage, distortion, and bending [3, 45]. This study investigates vertical displacements through experimental and numerical models, establishing four reference lines on the plate for distortion analysis, as shown in figure 3. Line 1 is positioned at x=0 mm, line 2 at x=1000 mm, line 3 is at y=0 mm, and line 4 at y=600 mm.

4.1. Validation of the numerical model

4.1.1. Validation of thermal model. The temperature histories for nodes T1 and T2 are recorded for 9 mm thick specimen welded by straight forward sequence (S1) technique as shown in figure 7. The temperature distribution history obtained through numerical simulations aligns closely with the experimental findings. Discrepancies between the numerical and experimental results are evident when the welding gun passes very close to measuring locations. One potential explanation for these differences is the influence of distance and the angle of measurement between the thermometer and the specimen at that time. This may affect the measurements and decrease their accuracy. When comparing these results to the experimental measurements, it has been noticed that temperature history is predicted with reasonable accuracy. The differences between the numerical and experimental

outcomes are deemed acceptable and it is concluded that the numerical models have been validated by the experimental data in the thermal analysis.

4.1.2. Validation of mechanical behaviour. The proposed methodology was validated by comparing numerical analysis results with experimental measurements. Vertical displacement along L1 for cases T9-S1 and T18-S1 is illustrated in figure 8. The results show a commendable agreement between the numerical and experimental data with deviations not exceeding 15% in all cases due to inhomogeneous material properties and dimensional inaccuracies.

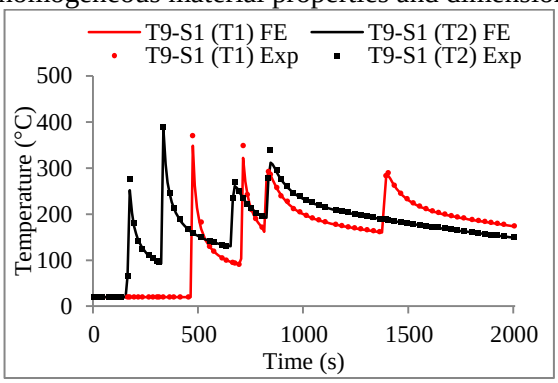

Figure 7. Temperature history comparison between the numerical and experimental data for T9-S1 model at T1 and T2 nodes.

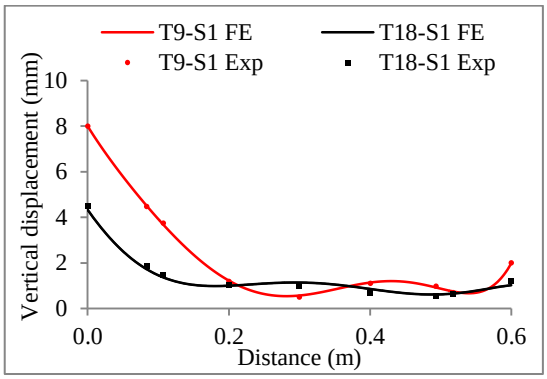

Figure 8. Vertical displacement comparison between numerical and experimental data for T9-S1 model along L1 (x=0 mm).

4.2. Influence of welding sequence and plate thickness on thermal distribution

Figures 9 and 10 present a comparison for temperature variation versus time among the four welding cases at T1 and T2 nodes, respectively. As indicated in the illustrations, significant dissimilarities in temperature values and distribution profiles among various welding sequences are observable when sequences and thicknesses are varied. For S1, the weld metal is deposited in an undivided pass along the welding line. Conversely, in S2, it is divided into two shorter segments. Additionally, under different thicknesses, temperature gradients exhibit different distribution patterns within the same sequences. It is also evident that the 9 mm thick cases endure the maximum peak temperatures reached during the welding process and higher cooling rates are also noted after welding process ends. A steeper temperature drop is also recognized between any two consecutive weld passes for the 9 mm thick plate. Furthermore, it can be deduced that the temperature distribution across the entire plate varies according to altering welding sequences. This differential thermal distribution significantly influences the deformation pattern and magnitude. The slower cooling rate in S1 effectively limits the extent of deformation by fostering a more uniform temperature distribution. In contrast, S2 experiences larger thermal gradients, raising the probability of warping and bending [46].

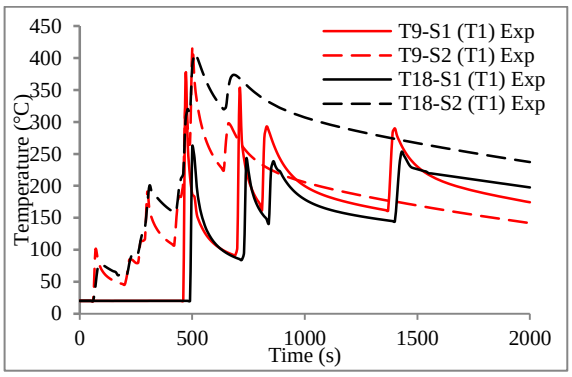

Figure 9. Temperature histories at node T1.

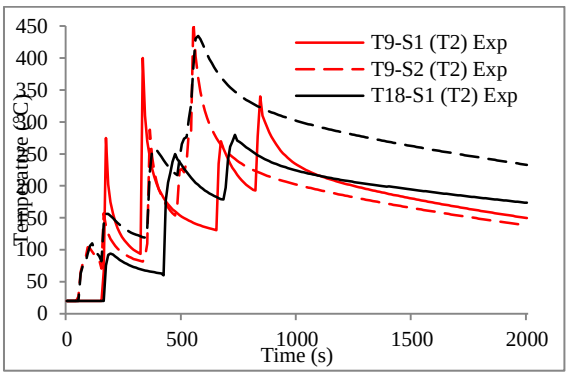

Figure 10. Temperature histories at node T2.

4.3. Influence of varying welding sequence and plate thickness on distortion distribution

Localized deformation in welded structures can be attributed to two primary causes, the first being the angular distortion of the fillet welds that leads to non-uniform contraction within the specimen along the thickness direction. This issue can be addressed by increasing the thermal rate in the heat-affected zone through various welding strategies such as optimized welding sequences, heat sinking, and flame heating. The second factor involves buckling deformation in the specimen that happened due to residual stresses generated by welding; this stress magnitude is governed by the total heat input from the welding operation [47].

To illustrate the effects of varying both welding sequences and plate thicknesses on distortions, vertical displacements recorded upon constraint removal are analysed. This occurs after attaining room temperature. The analysis is conducted for the four models, as demonstrated in figures 11, 12, 13, and 14 along lines 1, 2, 3, and 4, respectively. Linear deformation patterns extend from the weld to the transverse edges. Maximum deformations occur at the edges of the plate or at least at either one of the plate edges or vertices. This is shown in the simulated models T9-S1, T9-S2, T18-S1, and T18-S2 in figures 15. Notably, there is little deformation at the centre due to the presence of a manhole opening in the space between the two longitudinal stiffeners. It is pertinent to observe that the deformation differentials for various welding sequences at either or both edges of the plate surpass those identified at the centre. This indicates that welding sequences exert a sizable influence at the edges than at the centre. A summary of the maximum vertical displacements for nodes located along both transverse edges of the panel for each case is provided in table 7.

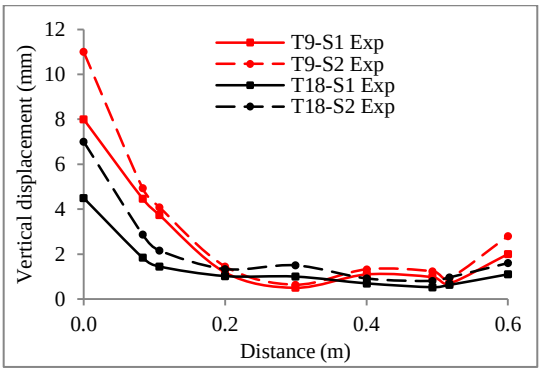

Figure 11. Measured vertical displacement along L1(x=0 mm).

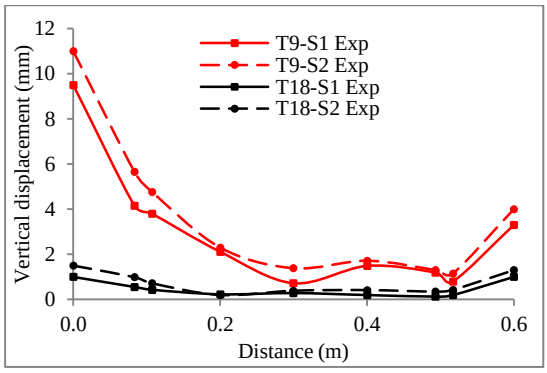

Figure 12. Measured vertical displacement along L2 (x=1000mm).

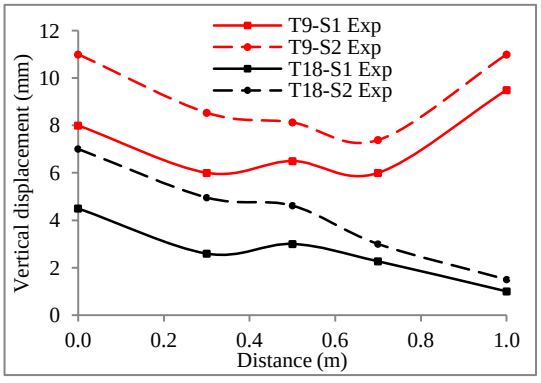

Figure 13. Measured vertical displacement along L3 (y=0 mm).

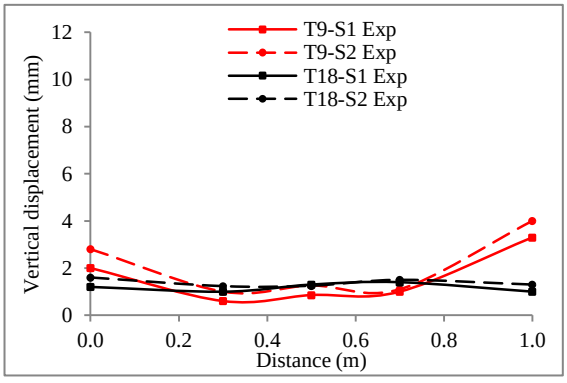

Figure 14. Measured vertical displacement along L4 (y=600 mm).

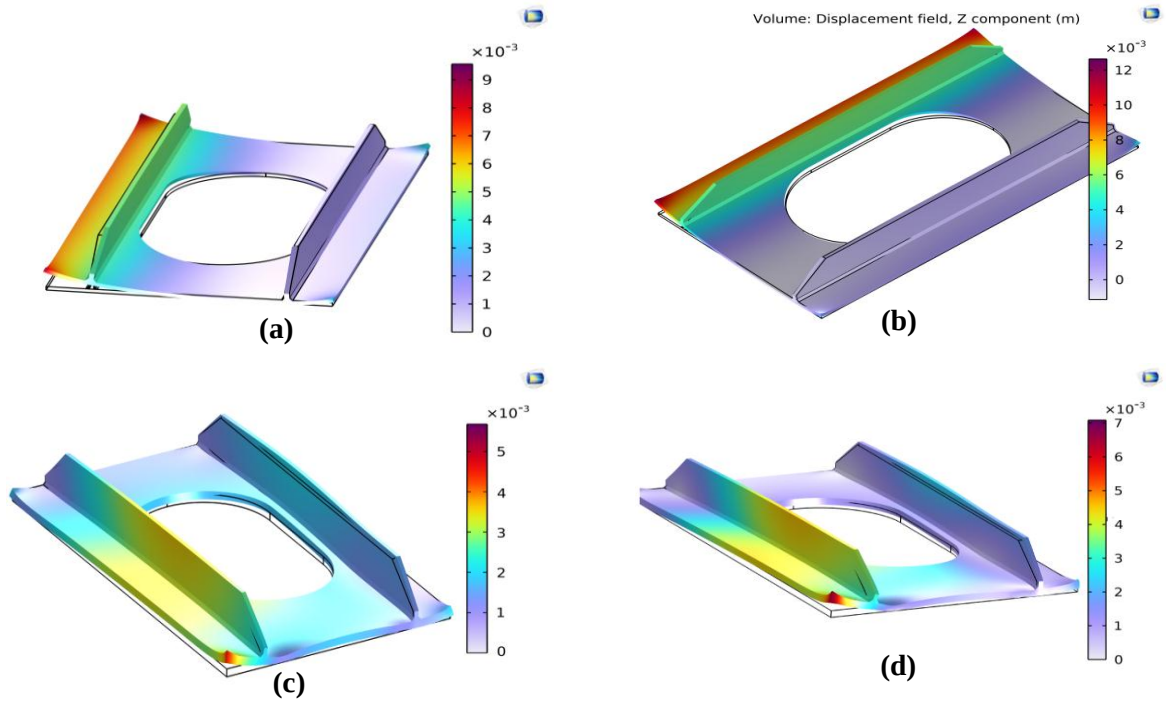

Figure 15. Simulated models vertical displacement. **(a)** T9-S1. **(b)** T9-S2. **(c)** T18-S1. **(d)** T18-S2.

The variation in sequences and plate thicknesses exert a significant influence on the ultimate distortion. This impact is further illustrated in table 7, based on the experimental measurements, which evidence that sequence alterations affect vertical displacement values. For the same thickness, at the four vertices of the plate, which are considered critical points during fabrication stages, S1 shows lower vertical displacement than S2. For a 9 mm thick plate, using S1 instead of S2 triggers a maximum reduction in vertical displacement (T9- S2 to S1) by 28.6%. This is a reduction from 2.8 mm for case T9-S2 to 2 mm for T9-S1. For the 18 mm thick plate (T18- S2 to S1), there is a 35.8% drop. This is a drop from 7 mm for case T18-S2 to 4.5 mm for T18-S1, which is the maximum displacement in the Z-axis. Although S1 shows a more notable impact than S2 in vertical distortion reduction, increasing plate thickness for the same sequence and approximately the same heat input has a greater impact on distortion reduction. When plate thickness increases from 9 mm to 18 mm, the reductions for (S1- T9 to T18) and (S2- T9 to T18) are 89.5%. This is a fall from 9.5 mm for case T9-S1 to 1 mm for T18-S1. For S2, the reduction is 86.4%, from 11 mm for case T9-S2 to 1.5 mm for T18-S2. These observations underscore the critical role of sequence variation in mitigating vertical displacement for thicker plates. This is even more significant than for thinner plates. Optimizing welding sequences, along with choosing an appropriate plate thickness, could largely mitigate vertical displacement for the plate during design and fabrication phases.

Table 7. Vertices displacement values and reduction percentages per sequence and thickness variation.

Vertices location	Cases				Reduction %			
	T9-S1	T9-S2	T18-S1	T18-S2	T9-S2 to S1	T18-S2 to S1	S1-T9 to T18	S2-T9 to T18
x=0,y=0	8	11	4.5	7	27.3	35.8	43.8	36.3
x=0,y=600	2	2.8	1.1	1.6	28.6	31.25	45	42.9
x=1000,y=0	9.5	11	1	1.5	13.6	33.3	89.5	86.4
x=1000, y=600	3.3	4	1	1.3	17.5	23.1	69.7	67.5

5. Conclusions

Distortion in welded assemblies is an unavoidable issue that necessitates effective management techniques. This study examines how different welding sequences, such as straight forward, S1, and centre-out to the edges, S2, affect vertical displacement. This is done in two different thicknesses of the stiffened plate with a manhole opening under similar constraining conditions.

A three-dimensional finite element (FE) model was built using COMSOL Multiphysics 6.0 to simulate the FCAW process for double-sided T-joints, with an emphasis on weld-induced distortions. The study employs a thermo-elastic-plastic framework to account for temperature-related material nonlinearity, and the simulation findings are validated experimentally. The key findings are as follows.

1) Numerical simulations properly predicted temperature distributions and angular deformations, validating the use of the finite element approach in welding distortion analysis. However, divergences were noted due to inconsistent material properties and process variables. Utilizing this approach can also lead to significant time and cost savings.

2) The straight sequence, S1, has a more uniform heating pattern. This leads to uniform temperature distribution and improved thermal gradients, thereby limiting deformation. In contrast, the centre-out sequence, S2, generates more elevated thermal gradients due to its welding path, increasing the risk of distortion.

3) S2 shows higher peak temperatures, sharper temperature drops, and faster cooling rates than S1, resulting in more vertical displacement in 9 mm and 18 mm thick plates.

4) Switching from S2 to S1 lowers vertical displacement by 28.6% for the 9 mm plate and 35.8% for the 18 mm plate, highlighting the effect of sequence variation in mitigating distortion, especially in thicker plates.

5) Increasing the plate thickness from 9 to 18 mm reduces displacement in the Z-axis more than the welding sequence does, with drops of 89.5% for S1 and 86.4% for S2. Furthermore, S1 outperforms S2 with respect to thickness variation.

6) S1 demonstrates greater time savings compared to S2 during and after welding. During welding, it saves approximately 11.31% and 13% of time for the 9 mm and 18 mm thick cases, respectively. Being more effective in reducing vertical distortion, S1 also leads to shorter post-welding distortion correction time using either thermal or mechanical techniques. These advantages enhance productivity, especially for large-scale shipbuilding and marine applications.

References

[1] Podder D, Gupta OP, Das S, Mandal NR 2019 Experimental and numerical investigation of effect of welding sequence on distortion of stiffened panels *Weld. World* **63** 1275–89

[2] Gannon L, Liu Y, Pegg N, Smith M 2010 Effect of welding sequence on residual stress and distortion in flat-bar stiffened plates *Mar. Struct.* **23** 385–404

[3] Deng D, Liang W, Murakawa H 2007 Determination of welding deformation in fillet-welded joint by means of numerical simulation and comparison with experimental results *J. Mater. Process. Technol.* **183** 219–25

[4] Arriaga IH, Aguilera GE, Pérez MJ 2016 Welding sequence analysis in three dimensional weldments with experimental verification *Memorias.*

[5] Chen BQ, Soares CG 2016 Effect of welding sequence on temperature distribution, distortions, and residual stress on stiffened plates *Int. J. Adv. Manuf. Technol.* **86** 3145–56

[6] Tsai CL, Park SC, Cheng WT 1999 Welding distortion of a thin-plate panel structure *Welding Res. Suppl.* **78** 157–65

[7] Park JU, An GB 2016 Effect of welding sequence to minimize fillet welding distortion in a ship's small component fabrication using joint rigidity method *Proc. IMechE, Part B: J. Eng. Manufacture* **230** 643–53

[8] Zhu J, Khurshid M, Barsoum Z 2019 Accuracy of computational welding mechanics methods for estimation of angular distortion and residual stresses *Welding in the World* **63** 1391–1405

[9] Keivani R, Jahazi M, Pham T, Khodabandeh A, Afshar M 2014 Predicting residual stresses and distortion during multisequence welding of large size structures using FEM *Int. J. Adv. Manuf. Technol.* **73** 409–19
[10] Seo JK, Yi MS, Kim SH, Kim BJ, Kim SJ 2018 Welding distortion design formulae of thin-plate panel structure during the assembly process *Ships Offshore Struct.* **13** 364–77
[11] Fu G, Estefen SF, Gurova T, Lourenço MI 2016 Influence of the welding sequence on residual stress and distortion of fillet welded structures *Mar. Struct.* **46** 30–55
[12] Deng D, Murakawa H, Ueda Y 2002 Theoretical prediction of welding distortion considering positioning and the gap between parts *The Twelfth International Offshore and Polar Engineering Conference*, International Society of Offshore and Polar Engineers, Hawaii **337**–43
[13] Mondal AK, Biswas P, Bag S 2017 Prediction of welding sequence induced thermal history and residual stresses and their effect on welding distortion *Weld. World* **61** 711–21
[14] Biswas P, Kumar DA, Mandal NR, Mahapatra MM 2011 A study on the effect of welding sequence in fabrication of large stiffened plate panels *J. Mar. Sci. Appl.* **10** 429–36
[15] Chen Z, et al. 2019 Comparative study of welding deformation of a stiffened panel under various welding procedures *Proc. Inst. Mech. Eng. B J. Eng. Manufacture* **233** 182–91
[16] Chen Z, Chen ZC, Shenoi RA 2015 Influence of welding sequence on welding deformation and residual stress of a stiffened plate structure *Ocean Eng.* **106** 271–80
[17] Shadkam S, Ranjbarnodeh E, Iranmanesh M 2018 Effect of sequence and stiffener shape on welding distortion of stiffened panel *J. Constr. Steel Res.* **149** 41–52
[18] Rodrigues LA, Borges DJ, Baia PE, Freitas EN, Braga EM 2019 Welding procedures influence analysis on the residual stress distribution and distortion of stiffened panels welded via robotized FCAW *Thin-Walled Struct.* **141** 175–83
[19] Azad N, Iranmanesh M, Rahmati Darvazi A 2020 A study on the effect of welding sequence on welding distortion in ship deck structure *Ships Offshore Struct.* **15** 355–67
[20] Hammad A, Abdel-Nasser Y, Shama M 2021 Rational design of T-girders via Finite Element Method *J. Mar. Sci. Appl.* **20** 302–16
[21] Tomk´ow J, Sobota K, Krajewski S 2020 Influence of tack welds distribution and welding sequence on the angular distortion of TIG welded joint *Facta Universitatis – Series: Mechanical Engineering* **18** 611–21
[22] Deng D, Liu XZ, He J, Liang W 2016 Investigating the influence of external restraint on welding distortion in thin plate bead-on joint by means of numerical simulation and experiment *Int. J. Adv. Manuf. Technol.* **82** 1049–62
[23] Aalami-aleagha ME, Eslampanah AH 2013 Mechanical constraint effect on residual stress and distortion in T-fillet welds by three-dimensional finite element analysis *Proc. Inst. Mech. Eng. B J. Eng. Manufacture* **227** 315–23
[24] Ma N, Huang H 2017 Efficient simulation of welding distortion in large structures and its reduction by jig constraints *J. Mater. Eng. Perform.*
[25] Liu J, Li Z, Ren S, Liang W, Deng D 2018 Investigating the mechanism of out-of-plane deformation in Q345 steel single-pass bead-on welded joint with external restraint *J. Mech. Eng.* **54** 90–7
[26] Fu G, Lourenço MI, Duan M, Estefen SF 2014 Effect of boundary conditions on residual stress and distortion in T-joint welds *J. Constr. Steel Res.* **102** 121–35
[27] Ma N, Huang H, Murakawa H 2015 Effect of jig constraint position and pitch on welding deformation *J. Mater. Process. Technol.*
[28] Liang W, Hu X, Zheng Y, Deng D 2020 Determining inherent deformations of HSLA steel T-joint under structural constraint by means of thermal elastic plastic FEM *Thin-Walled Struct.* 106568
[29] Woo DH, Kitamura M, Takezawa A 2020 Systematic method for positioning clamps and strongbacks based on their influence on welding displacements *Ocean Eng.* 202 107084

[30] Zhang Y, Wang Y 2019 The influence of welding mechanical boundary condition on the residual stress and distortion of a stiffened panel *Mar. Struct.* **65** 259–70
[31] Saad-Eldeen S, Eltaramsy M A, Mansour M 2024 Distortion Analysis of Steel Stiffened Plates Accounting for Different Welding Configurations *Port-Said Engineering Research Journal* **28** 132-139
[32] Ghafouri M, et al. 2022 Mechanical properties of butt-welded ultra-high strength steels at elevated temperatures *J. Constr. Steel Res.* **198** 107499
[33] Seleš K, Perić M, Tonković Z 2018 Numerical simulation of a welding process using a prescribed temperature approach *J. Constr. Steel Res.* **145** 49–57
[34] Izeda AE, Pascoal A, Simonato G, Mineiro N, Gonçalves J, Ribeiro JE 2018 Optimization of robotized welding in aluminum alloys with pulsed transfer mode using the Taguchi method *Proceedings* **2** 426
[35] Prajadhiana KP, et al. 2020 Investigation on welded T-joint distortion using virtual manufacturing tools with simplified procedure *J. Korean Soc. Precis. Eng.* **37** 91–97
[36] Nateghi E, Volukola AG 2019 Numerical and experimental investigations of trajectory effects into temperature distribution and distortion in the slot welding of steel S235JR *Int. J. Steel Struct.* **19** 819–33
[37] Goldak J, Chakravarti A, Bibby M 1984 A new finite element model for welding heat sources *Metall. Trans. B* **15** 299–305
[38] Ghafouri M, Ahola A, Ahn J, Björk T 2022 Numerical and experimental investigations on the welding residual stresses and distortions of the short fillet welds in high strength steel plates *Eng. Struct.* **260** 114269
[39] Deng D 2009 FEM prediction of welding residual stress and distortion in carbon steel considering phase transformation effects *Mater. Des.* **30** 359–66
[40] Ma N, Cai Z, Huang H, Deng D, Murakawa H, Pan J 2015 Investigation of welding residual stress in flash-butt joint of U71Mn rail steel by numerical simulation and experiment *Mater. Des.* **88** 1296–309
[41] Li Z, et al. 2021 Investigating welding distortion of thin-plate stiffened panel steel structures by means of thermal elastic plastic finite element method *J. Mater. Eng. Perform.* **30** 3677–90
[42] Sun J, Liu X, Tong Y, Deng D 2014 A comparative study on welding temperature fields, residual stress distributions and deformations induced by laser beam welding and CO2 gas arc welding *Mater. Des.* **63** 519–30
[43] Ahn J, He E, Chen L, Wimpory RC, Dear JP, Davies CM 2017 Prediction and measurement of residual stresses and distortions in fibre laser welded Ti-6Al-4V considering phase transformation *Mater. Des.* **115** 441–57
[44] Deng D, Murakawa H 2008 Prediction of welding distortion and residual stress in a thin plate butt-welded joint *Comput. Mater. Sci.* **43** 353–65
[45] Deng D, Zhou Y, Bi T, Liu X 2013 Experimental and numerical investigations of welding distortion induced by CO2 gas arc welding in thin-plate bead-on joints *Mater. Des.* **52** 720–29
[46] O'Brien T, et al. 2014 Welding distortion control: A review *Welding J.* **93** 132S–139S
[47] Wang J, Yin X, Murakawa H 2013 Experimental and computational analysis of residual buckling distortion of bead-on-plate welded joint *J. Mater. Process. Technol.* **213** 1447–58